Journal of Power Sources 206 (2012) 343–348

Contents lists available at SciVerse ScienceDirect

Journal of Power Sources

journal homepage: www.elsevier.com/locate/jpowsour

The influence of particle size and spacing on the fragmentation of nanocomposite anodes for Li batteries

B.J. Dimitrijevic[a], K.E. Aifantis[b,*], K. Hackl[a]

[a] Mechanik-Materialtheorie, Ruhr-Universität Bochum, D-44801 Bochum, Germany
[b] Department of Physics, Michigan Technological University, Houghton, MI 49931, USA

ARTICLE INFO

Article history:
Received 19 October 2011
Received in revised form 6 January 2012
Accepted 7 January 2012
Available online 17 January 2012

Keywords:
Nanocomposite anodes damage
Li batteries
Fracture
Graphene

ABSTRACT

Experimental evidence has shown that composites comprised Si and Sn nanoparticles embedded inside a matrix are the most promising next generation anodes for Li-ion batteries. This is due to the ability of the matrix material to constrain/buffer the up to 300% volume expansion that Sn and Si undergo upon the formation of lithium rich alloys. Damage still occurs at the nanoparticle/matrix interface, and hence further materials design is required in order to commercialize such anodes. Initial theoretical works have predicted that low volume fractions and high aspect ratios of the nanoparticles result in a greater mechanical stability and hence better capacity retention. The most important design parameters, however, such as particle size and spacing have not been considered theoretically. In the present study, therefore, a gradient enhanced damage model will be employed to predict that damage during Li-insertion, is negligible when the particle size is 20 nm, and the interparticle half-spacing greater then 1.5 times the particle diameter. Furthermore, from the matrix materials considered herein graphene is predicted to be the most promising matrix, which is consistent with recent experimental data.

1. Introduction

In trying to develop Sn and Si based anodes, for secondary Li-ion batteries, it has been shown that configuration and geometric parameters drastically affect their electrochemical performance. This is due to the fact that, upon the formation of Li-rich alloys, Sn and Si expand 300%, which leads to fracture; hence the efficiency of the anode depends on its ability to withstand these volume changes. Experimental research has shown that fracture is minimized when the active material with respect to Li has dimensions in the nanoscale [1,2], while further mechanical stability is obtained by embedding the nanoparticles in a matrix in order to constrain and buffer their expansion [3]. It has been shown for example that embedding Si nanoparticles in carbon allowed for a capacity retention of 1000 $mAhg^{-1}$ for twenty cycles [4], while attaching Si nanoparticles on cellulose gave a capacity retention of 1400 $mAhg^{-1}$ for fifty cycles [5]. Furthermore, embedding Sn nanoparticles in carbon allowed for a capacity of 500 $mAhg^{-1}$ for 100 cycles and attaching Sn on cellulose resulted in a capacity of 500 $mAhg^{-1}$ for forty cycles [6]. Not all Si and Sn based nanocomposites, however, exhibit such good capacity retentions, since the volume expansions of the Si within the composite can result in severe fracture in most cases [7,8]. As a result the capacity decreases significantly, since fracture limits the connectivity in the anode, and active material can be lost in the electrolyte. Although models have been developed that correlate the active site volume change to the resulting capacity [9], it is not possible to obtain a material selection that provides a promising capacity without a significant volume expansion [10]. It is, therefore, important to develop theoretical models that can predict damage in nanocomposite anodes.

Linear elastic fracture mechanics have been employed to predict the stable configurations [11] and to develop design criteria for selecting the matrix material and determining the preferable volume fractions of the active site that will limit fracture [12]. These studies indicated that increasing the volume fraction and decreasing the aspect ratio of the Sn or Si will result in greater instabilities during fracture, and this was consistent with experimental observations [13]. A more detailed correspondence, however, between damage and capacity showed that the capacity strongly depends on the area fraction and volume average of the active particles [14]. Hence, the most important geometric parameters that must be considered are the explicit size of the Sn particles and their spacing.

In doing so, standard continuum mechanics studies, as those employed thus far [11–13] for studying anodes, cannot be used, as they cannot account for the specimen microstructure and scale. Instead gradient theories must be utilized. The unique feature of gradient theories is that they explicitly consider the scale of the microstructure, by introducing a characteristic length unique to the material at hand. Since the damage that occurs in Sn/C anodes resembles crumbling [14], i.e. a mode of distributed damage, the

* Corresponding author. Tel.: +30 6936208504; fax: +30 2310 995921.
E-mail addresses: kaifanti@mtu.edu, k.aifantis@mom.gen.auth.gr (K.E. Aifantis).

0378-7753/$ – see front matter © 2012 Elsevier B.V. All rights reserved.
doi:10.1016/j.jpowsour.2012.01.065

most appropriate model to capture this behavior is that of gradient enhanced damage mechanics. In this model the properties of the matrix govern the damage behavior and, therefore, a variety of materials will be considered, similarly as in [12], in order to determine which material selection exhibits minimum damage. Then the extent of damage will be computed for different radii of the Si or Sn particles, providing information for the optimum inter-particle spacing. It is noted that in fabricating anodes the above mentioned Sn and Si based nanocomposites are mixed with C black and PVDF; in the present study the effects of these additives to the mechanical stability are not considered, as the main factor resulting in capacity decay is fracture of the Sn or Si [11,14].

2. Theoretical approach

2.1. Damage material model

One defines damage as the alteration of any material physical property due to the presence or the nucleation/growth of defects (microcracks, voids, delamination, etc.). In order to characterize, represent and model at the macroscopic scale the effects of such distributed defects and their growth on the material behavior, various continuum damage models have been developed. These models use a set of continuous damage variables that are supposed to describe aspects of the internal material structure associated with the irreversible (dissipative) effects. According to the pretty wide and abstract definition of the phenomena they describe, there is a variety of damage variables used in literature, ranging from scalars over first-, second-, forth-, up to eighth-order tensors. A survey on this subject can be found in [15–18]. The evolution of damage, meaning (i) the nucleation of new microcracks resulting in distributed microcracking, as well as (ii) the propagation (growth) of already existing microcracks, induces anisotropy even in initially isotropic materials. However, in a lot of problems it is sufficient, at least from the phenomenological point of view, to assume that the development of damage does not affect material isotropy, since the microcracks can be randomly oriented so that no preferable direction exists or the microvoids have a spherical shape and isotropic distribution. In these cases scalar damage variables adequately describe the local state of a damaged material. Two classical interpretations of this approach can be given. The first one (cf. [15]) represents the ratio between the area dA_D of the intersection of all microcracks and microvoids with the total area dA of the plane section $D = dA_D/dA$. The second one (cf. [16]) represents the current volume fraction of the voids in the representative volume element $D = dV_P/dV$.

From both definitions it follows that $D \in [0, 1]$, where $D = 0$ stands for the undamaged material and $D = 1$ represents maximum damage and hence complete loss of integrity. For further details on the subject of continuum damage mechanics one is referred to [17,18].

2.2. A gradient-enhanced damage material model

In order to account for the scale of the microstructure [19], a damage material model including a regularization strategy based on gradient enhancement [19] of the free energy function is used in the present study. The enhancement is formulated through an interaction potential [20–22], which depends on a newly introduced variable field and its gradients

$$\tilde{\psi} = \frac{1}{2}\, f(d)\ (\boldsymbol{\epsilon} : \mathbb{C} : \boldsymbol{\epsilon}) + g(d) + \frac{c_d}{2}\|\nabla\varphi_d\|^2 + \frac{\beta_d}{2}[\varphi_d - H_\varphi(d)]^2, \quad (1)$$

where β_d represents the energy penalizing the difference between the corresponding non-local and local fields, c_d stands for the gradient parameter which implicitly introduces a damage internal material length, which can be shown to be

$$L_d^2 = \frac{c_d}{\beta_d}, \quad (2)$$

and $H_\varphi(d)$ represents an appropriate interaction function. The parameter L_d describes the size of the damage localization zone, cf. [19,23,24]. The scalar variable d measures the degree of material stiffness loss and is monotonically related to the damage ratio (reduction of the Young's modulus)

$$f(d) = \frac{E_c}{E_0}, \quad (3)$$

where E_c stands for the current effective Young's modulus (or better named secant stiffness modulus) that corresponds to the particular damage state and E_0 represents its initial value. Strictly speaking, the initial material always contains some defects, but it is assumed that these are accounted for in the virgin material properties. The total energy Π is obtained in standard manner as the difference between the potentials of internal and external body forces $\mathbf{b}$ and traction forces $\mathbf{t}$ as

$$\Pi = \Pi_{int} - \Pi_{ext} = \int_\Omega \tilde{\psi}(\boldsymbol{\epsilon}, d, \varphi_d, \nabla\varphi_d)dV - \int_\Omega \mathbf{u}\cdot(\rho\mathbf{b})\,dV - \int_{\partial\Omega_\sigma} \mathbf{u}\cdot\mathbf{t}dA. \quad (4)$$

Field equations for $\mathbf{u}$ and φ_d can now be obtained by minimizing Π with respect to these variables:

$$\text{find}\ \{\mathbf{u}, \varphi_d\} = \text{argmin}\ \{\Pi(\mathbf{u}, \varphi_d) | \mathbf{u} = \mathbf{u}^* \text{ on } \partial\Omega_u\}, \quad (5)$$

where the internal variable d is considered constant with respect to variation, for details see [20–22].

Following common thermodynamic considerations, the damage driving force is defined by the enhanced free energy function Eq. (1) as the conjugate quantity of the governing variable:

$$\eta_d = -\frac{\partial\tilde{\psi}}{\partial d}. \quad (6)$$

The evolution of the damage in time is determined by a damage potential ϕ_d as

$$\dot{d} = \dot{\kappa}\ \frac{\partial\phi_d}{\partial\eta_d}; \qquad \dot{\kappa} \geq 0, \quad \phi_d \leq 0, \dot{\kappa}\phi_d = 0, \quad (7)$$

where $\dot{d}$ represents the rate of the damage variable and $\dot{\kappa}$ stands for the rate of the consistency parameter. The detailed form of ϕ_d employed in this work is given in Appendix A. Differential-algebraic inequalities as given by Eq. (7) are common in the modeling of inealstic materials, see e.g. [25].

Eqs. (5) and (7) now completely determine our problem. For details on the solution procedure, see once again [20–22].

2.3. Geometries considered

Based on experimental evidence [4], the active sites are treated as spherical inclusions embedded periodically inside a matrix (this approach was also followed in previous theoretical modeling [28,11,3]), as illustrated in Fig. 1. Considering spherical symmetry allows for the 3D problem to be reduced to a two-dimensional axisymmetric configuration, cf. [29]. In order to reduce the computational effort necessary to perform the damage analysis, the originally rectangular unit-cell is replaced by a cylindrical one, see Fig. 1. That way, a small error is introduced which, however, is certainly smaller than that one due to the difference between regular and random distributions and thus has no significant influence on the results in general [30]. The unit cell problem is then solved for

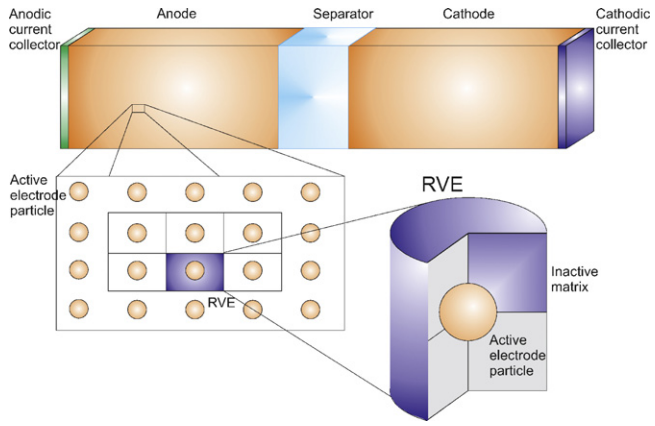

Fig. 1. Geometry of the electrode and a representative volume element.

periodic boundary conditions , by which one displacement direction is equal to zero at the outer boundary of the unit cell as shown in Fig. 2a; therefore, the effect of a neighboring nanoparticle can be accounted for. For purposes of comparison the case of clamped boundary conditions (Fig. 2b) is also considered by letting both displacement components be zero at the outer boundary of the unit cell. The geometry of the representative volume element and consequently the matrix geometry is assumed to be cylindrical. The volume expansion of the Li inclusion is applied as a uniform displacement in the radial direction; hence a 300% volume expansion corresponds to a 58.74% increase of the inclusion radius. Therefore, it will be assumed that the diameter increases by 1/3 during maximum Li-insertion, which corresponds to a 237.5% volume increase in the radial direction. The behavior of a material at such large volume changes cannot be very accurately described using a small-strain material model. However, it can give first insights into the problem of the evolution of damage in the matrix material surrounding the Li-active inclusion. The analysis formulated in the present paper is based on large-strain considerations.

As mentioned in Section 2.2 the damage model employed here is sensitive to the material parameters of the matrix, hence by computing the damage that results for various matrix materials, the most promising matrix can be selected. In order to be able to compare with the predictions of earlier studies [12], the same materials as those considered in [12] (Al_2O_3, B_4C, BeO, WC, [31]) will also be considered here; it should be noted that such materials are not used in actual anodes. Therefore, in addition to those materials, Cu [32] and graphene [33] will be treated here, since they have been explicitly employed as matrix materials in nanocomposite anodes. Cu has been used as the matrix with Sb [35] or Sn as the active sites [34] (upon lithiation, the Sn–Cu or Sb–Cu intermetallic compounds decompose into Sn and Sb nanoparticles dispersed in the inert Cu matrix). More recently, graphene has been recently employed as the matrix in Sn-based anodes and was shown to

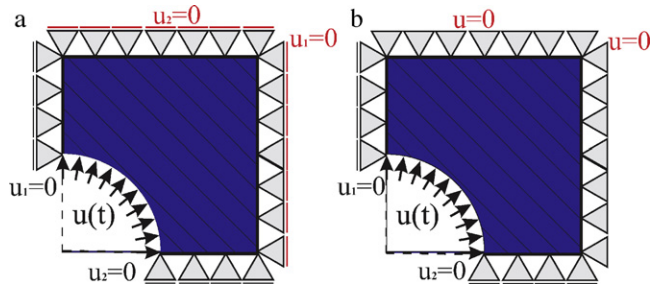

Fig. 2. Numerical analysis model including periodic (a) and clamped (b) boundary conditions.

Table 1
Material parameters for various ceramic matrices (E: Young's modulus, ν: Poisson's ratio, f_t: uniaxial tensile strength).

Material	E (GPa)	ν	f_t (MPa)
Al_2O_3	345.0	0.23	255.0
B_4C	450.0	0.21	155.0
BeO	400.0	0.24	246.0
WC	700.0	0.24	345.0
Cu	130.0	0.355	210.0
Graphene	1000.0	0.4	130000.0

Table 2
Material parameters of the gradient damage model.

c_d (GPa nm^2)	β_d (GPa)	α_1
400.0	100.0	1.5

be very effective, allowing for good capacity retentions above 550 mAhg^{-1} [36–38]; it is noted that graphene on its own has a low capacity 300 mAhg^{-1}. Although Sn/graphene anodes are not nanocomposites in the traditional sense, as graphene has a layered structure, based on TEM images [36] it can be seen that Sn nanoparticles are fully surrounded by graphene and therefore the configuration employed in the present study (nanoparticles surrounded by a matrix) can be used to model damage in such systems. Furthermore, the authors of [36] also refer to such Sn/graphene systems as nanocomposites. An experimental measure for the elastic modulus of graphene does not exist and therefore the value computed by MD simulations [33] will be employed. Inserting these values into Eq. (6) provides an internal length of 2 nm.

3. Results and discussion

To illustrate the development of damage for the various material systems considered, the results will be presented by plotting the damage ratio, given in Eq. (3), over the radial distance from the inclusion. The results presented are obtained for the volume expansion of the active site of 237.5%, which corresponds to an increase in diameter of the inclusion of 1/3 of its original size.

In order to investigate the behavior of different materials which can be used as an anode matrix, a series of simulations were performed by fixing the radius of the spherical inclusion at 100 nm and the half-distance between inclusion centers at 1000 nm. The elastic material parameters and the corresponding tensile strength are listed in Table 1. The parameters specific to the damage model and

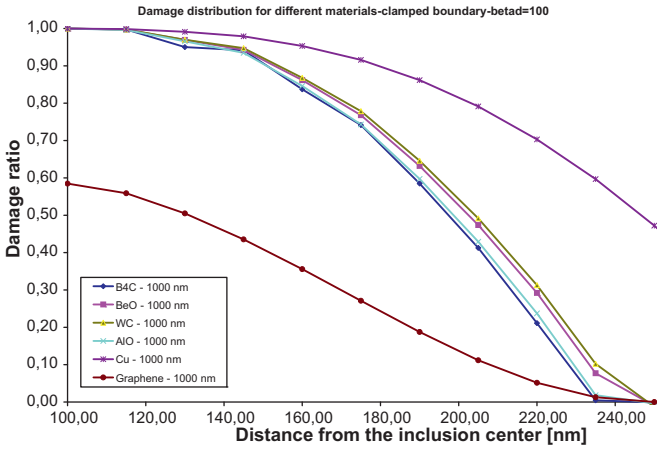

Fig. 3. Damage distribution along the radial distance from the inclusion center for different materials of the surrounding matrix.

used in the gradient-enhancement strategy are listed in Table 2; inserting these values in Eq. (2), gives an internal length of 2 nm.

In Fig. 3 it is seen that the damage is always highest at the active site–matrix interface since that is where the highest tensile stresses are present, and as the distance from this interface increases the damage decreases. From Fig. 3 it is predicted that from the various matrix materials examined, the use of Cu results in the highest damage, while graphene in the least damage, which would be expected considering graphene's layered structure, and the resulting ability to accommodate the expansion of the active sites (such as Si, Sn). These theoretical predictions are in agreement with experimental data, since when Cu is used as the matrix in Sn–Cu anodes the capacity retention is not improved over the pure Sn anodes, indicating that Cu is not effective in buffering the Sn volume expansions [34]. Using graphene, however, as the matrix in Sn–C anodes allows for stable capacity retention over 500 mAhg^{-1} [38], suggesting a high mechanical stability.

Concerning the remaining materials considered (Al_2O_3, B_4C, BeO, WC), it is interesting to note that B_4C is the most promising, and this is consistent with the predictions in [12]. It should be noted that in the model employed here damage depends on the ratio of the material parameters

$$r_1 = \frac{f_t^2(1-\nu)}{E(1-2\nu)(1+\nu)}. \quad (8)$$

Hence, any material which has a ratio similar to that of graphene would be a promising matrix candidate, whereas materials with r_1 similar to that of Cu should be avoided. Of course, detailed experimental studies should be performed in order to determine the material parameters for materials at the nanoscale.

Since graphene is the most promising matrix, its parameters will be used in the sequel as we proceed to examine the influence of microstructure. In order to investigate the influence that particle spacing has on anode stability a new set of simulations is performed in which the radius of the inclusion is kept constant at 100 nm, but the matrix radius/half spacing between neighboring inclusions is allowed to attain the values of 200 nm, 300 nm, 500 nm or 1000 nm.

In Fig. 4 we illustrate that the damage tends to 0 once the distance from the inclusion center reaches 250 nm, provided the interparticle spacing is large enough. However, for a small matrix radius of 200 nm damage extends to the next neighboring particle, and therefore the anode fractures completely. This means that for nanoparticles of the size considered here a larger interparticle distance gives greater mechanical stability, which is consistent with the earlier prediction that lower active site volume fractions allow for higher stability [12]. Furthermore, in Fig. 4 it is seen that periodic boundary conditions result in higher damage than the clamped boundary conditions. However, it can be concluded that, at least for

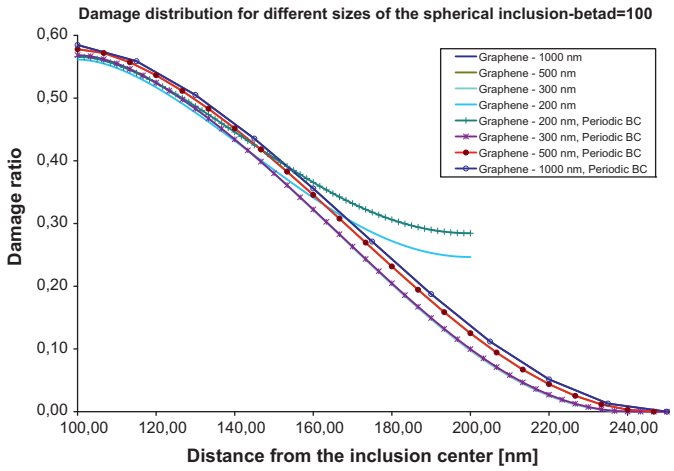

Fig. 4. Damage distribution along the radial distance from the inclusion center for different half-distance between inclusion centers and inclusion radius of 100 nm.

this model, boundary conditions play a role only if the interparticle half-distance (matrix radius) is quite small since at spacings larger than 1.5 up to 3 times the particle diameter both boundary conditions give overlapping results.

In order to better illustrate the effect of interparticle spacing, the distribution of the "material damage", defined as percentage of the material stiffness loss MD [%] = $(1.0 - f(d)) \times 100$ for two different cases of interparticle spacing are given in Fig. 5. It is seen that the size and shape of the damage zone is highly influenced by the interparticle spacing and the interaction between the corresponding damage zones. Particularly, for small interparticle spacing, when the damage zones between the particles interact (according to Fig. 4), damage is highly non-uniform, whereas for large interparticle spacing damage appears to be radially symmetric.

In addition to considering particle size and spacing, it is of interest to examine volume fraction effects. In [12] it was shown that smaller volume fractions result in a greater difficulty for cracks to propagate. In Fig. 6, however, it is illustrated that keeping the volume fraction constant, while varying the inclusion radii and distances, results in significant differences. It is seen that reducing the inclusion radius below 20 nm causes a decrease of the maximum damage, but proportionally wider spreading of the damaged zone. For example, although the damage ratio is smallest when the inclusion radius is 20 nm, 50% of the matrix is damaged, whereas when the inclusion radius is 100 nm, the maximum damage ratio is higher, but only 25% of the matrix is damaged. This phenomenon is due to the fact that in the former case the interparticle spacing

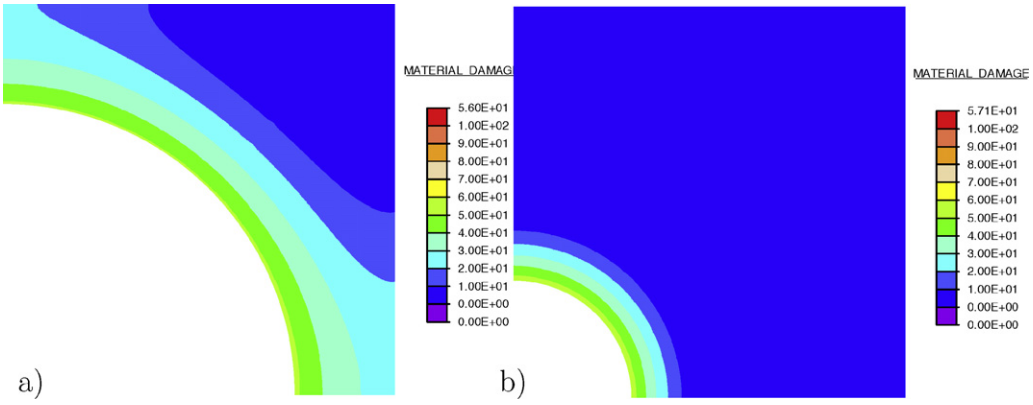

Fig. 5. Damage distribution for inclusion radius of 100 nm and half-distance between inclusion centers of 133 nm (a) and 400 nm (b) for the case with periodic boundary conditions.

Table 3
Summary of results when graphene is used as matrix.

Particle diameter (nm)	Inter-particle spacing (nm)	Width of damage zone in matrix starting from the interface with active site (nm)	Damage ratio (initial and end values)
20	40	10	0.48–0.478
20	60–100	20–25	0.065–0
40	80	20	0.49–0.48
80	160	40	0.5–0.45
200	400–2000	240	0.6–0

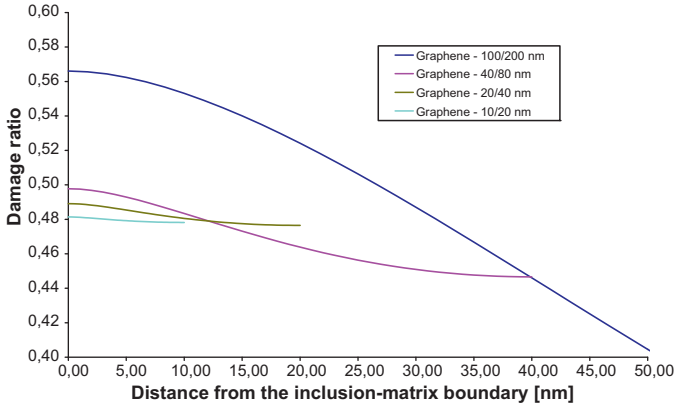

Fig. 6. Damage distribution along the radial distance from the inclusion–matrix boundary for different inclusion radii and distances, and fixed volume matrix–inclusion ratio (first number: inclusion radius, second number: half-distance between inclusion centers).

becomes comparable to the internal material length given in Eq. (2) which defines the size of the damaged zone.

In concluding these calculations it is of interest to produce a figure similar to Fig. 4, but for a smaller particle size. In Fig. 7, therefore, the inclusion radius is kept constant at 10 nm and the half-distance between inclusion centers is varied between 20 and 50 nm, to allow for similar volume fractions as in Fig. 4. In comparing Figs. 4 and 7 it is seen that when the inclusion radius is for example 100 nm the maximum damage ratio has the same value regardless of interparticle spacing, whereas when the inclusion radius is 10 nm the maximum damage ratio becomes practically negligible once the particle half-spacing is 1.5 times larger than the particle diameter. This explicitly illustrates the significant effect that inclusion size has in the mechanical and hence electrochemical stability of anodes. Table 3 summarizes the predictions that the theoretical

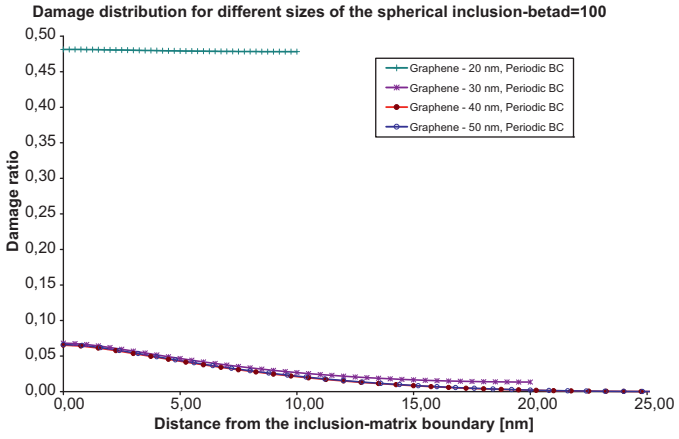

Fig. 7. Damage distribution along the radial distance from the inclusion–matrix boundary for different values of the half-distance between inclusion centers and inclusion radius 10 nm.

model gives (in Figs. 5–7) for a graphene matrix with different particle sizes and interparticle spacings. It is noted that in the figures presented the particle radius is stated, along with the radius of the surrounding matrix, while in this table the spacing between two particles is given, which is twice the matrix radius.

4. Conclusions

The present study employs a gradient dependent damage model to explicitly account for the effect that Sn or Si volume fractions, particle size and spacing have in the stability of nanocomposite anodes. It is illustrated that when the interparticle spacing is comparable to the particle size the damage is non-uniform, whereas when the interparticle spacing is large the damage is localized and radially symmetric. Furthermore, it is shown that when the particle size is 20 nm and the interparticle half-spacing greater than 30 nm, the damage during Li-insertion is negligible. Therefore, it can be concluded that an optimal microstructure would consist of particles with diameters of 20 nm or below and interparticle spacings at least 1.5 times their diameter. Finally, it should be noted that by considering various matrix materials, it is shown that least damage occurred when the ratio of the material parameters specified in Eq. (8) is equal to that obtained for graphene, while it is worst when it is equal to that for Cu.

Acknowledgments

KEA would like to thank the European Research Council Starting Grant 211166 MINATRAN. BJD and KH gratefully acknowledge support by the German Science Foundation (DFG) within the Collaborative Research Centre SFB 526 'Rheology of the Earth'.

Appendix A.

In order to solve the differential-algebraic system Eq. (7) the evolution equation for damage is discretized in time employing a Backward-Euler scheme. In the present contribution a damage material model sensitive to tension is used. To achieve this task, a decomposition of the strain tensor into a "positive" (ϵ^+) and "negative" (ϵ^-) part is introduced

$$\boldsymbol{\epsilon}^+ = \sum_{i=1}^{3} \frac{1}{2} \left(\varepsilon_i + |\varepsilon_i|\right) \boldsymbol{n}_i \otimes \boldsymbol{n}_i; \qquad \boldsymbol{\epsilon}^- = \sum_{i=1}^{3} \frac{1}{2} (\varepsilon_i - |\varepsilon_i|) \boldsymbol{n}_i \otimes \boldsymbol{n}_i, \quad (9)$$

where ε_i stands for the eigenvalues of the strain tensor, while $\boldsymbol{n}_i$ stand for the corresponding eigenvectors. A thermodynamically consistent formulation of the threshold condition dependent on the positive part of the strain tensor has been developed by [26] and subsequently used by e.g. [27,21,23]. Here it assumes the form

$$\phi_d := \eta_d - \frac{1}{2}(-f\prime(d))(\boldsymbol{\epsilon}^- : \mathbb{C} : \boldsymbol{\epsilon}^- + 2\boldsymbol{\epsilon}^+ : \mathbb{C} : \boldsymbol{\epsilon}^-) \leq 0. \quad (10)$$

In the numerical examples in the rest of the paper the following softening function and damage potentials are used

$$f(d) = (1-d)^2, \qquad g(d) = \frac{1}{a_1}\ r_1\ \frac{1}{(1-d)^{a_1}}, \qquad H_\varphi(d) = g(0) - g(d), \tag{11}$$

where r_1 is a model material parameter that represents the damage threshold, and the parameter a_1 controls the rate of softening.

References

[1] H. Li, X.J. Huang, L.Q. Chen, Z.G. Wu, Y. Liang, Electrochem. Solid-State Lett. 2 (1977) 547.
[2] G.W. Zhou, H. Li, H.P. Sun, D.P. Yu, Y.Q. Wang, X.J. Huang, L.Q. Chen, Z. Zhang, Appl. Phys. Lett. 75 (1999) 2447.
[3] K.E. Aifantis, S.A. Hackney, R.V. Kumar (Eds.), High Energy Density Lithium Batteries: Materials, Engineering, and Applications, Wiley–VCH, 2010.
[4] Z. Wen, X. Yang, S. Huang, J. Power Sources 174 (2007) 1041.
[5] J.L. Gomez Gamer, J. Morales, L. Sanchez, Electrochem. Solid-State Lett. 11 (2008) A101.
[6] A. Caballero, J. Morales, L. Sanchezz, Electrochem. Solid-State Lett. 8 (2005) A464.
[7] Y.S. Jung, K.T. Lee, S.M. Oh, Electrochim. Acta 52 (2007) 7061.
[8] H. Yang, P. Fu, H. Zhang, Y. Song, Z. Zhou, M. Wu, L. Huang, G. Xu, J. Power Sources 174 (2007) 533.
[9] M.N. Obrovac, L. Christensen, D.B. Le, J.R. Dahn, J. Electrochem. Soc. 154 (2007) A849.
[10] Y. Tian, A. Timmons, J.R. Dahn, J. Electrochem. Soc. 156 (2009) A187.
[11] K.E. Aifantis, J.P. Dempsey, J. Power Sources 143 (2005) 143.
[12] K.E. Aifantis, S.A. Hackney, J.P. Dempsey, J. Power Sources 165 (2007) 874.
[13] K.E. Aifantis, S.A. Hackney, J. Power Sources 196 (2011) 2122.
[14] K.E. Aifantis, M. Haycock, P. Sanders, S.A. Hackney, Mater. Sci. Eng. A 529 (2011) 55.
[15] I.N. Rabotnov, Proceedings of the 12th International Congress of Applied Mechanics, 1968, p. 342.
[16] A. Gurson, J. Eng. Mater. Tech. 99 (1977) 2.
[17] D. Krajcinovic, Damage Mechanics, Elsevier, North-Holland, 2002.
[18] J. Skrzypek, A. Ganczarski, Modeling of Material Damage and Failure of Structures, Springer Verlag, Berlin, 1999.
[19] (a) E.C. Aifantis, J. Eng. Mater. Tech 106 (1984) 326;
(b) D. Bammann, E.C. Aifantis, J. Nucl. Eng. and Design 116 (1989) 355;
(c) E.C. Aifantis, Int. J. Eng. Sci 30 (1992) 1279.
[20] B.J. Dimitrijevic, K. Hackl, in: M. Kojic, M. Papadrakakis (Eds.), Proceedings of First South-East European Conference on Computational Mechanics, University of Kragujevac, 2006, p. 191.
[21] B.J. Dimitrijevic, K. Hackl, Tech. Mech. 28 (2008) 43.
[22] B.J. Dimitrijevic, K. Hackl, Int. J. Numer. Meth. Biomed. Eng. 27 (2011) 1199.
[23] B.J. Dimitrijevic, On a regularization framework for inelastic material models via gradient enhancement of the free energy function, PhD thesis, Ruhr-University of Bochum, 2010.
[24] S. Forest, J. Eng. Mech. 135 (2009) 117.
[25] J.C. Simo, T.J.R. Hughes, Computational Inelasticity, Springer Verlag, New York, 1998.
[26] M. Frémond, B. Nedjar, Int. J. Sol. Struct. 33 (1996) 1083.
[27] J. Makowski, K. Hackl, H. Stumpf, Int. J. Sol. Struct. 43 (2006) 3940.
[28] K.E. Aifantis, S.A. Hackney, J. Mech. Behav. Mater. 14 (2003) 413.
[29] K. Siruguet, J.-B. Leblond, Int. J. Plast. 20 (2004) 255.
[30] T.I. Zohdi, P. Wriggers, Int. J. Numer. Meth. Eng. 50 (2001) 2573.
[31] J.F. Shackelford, W. Alexander, CRC Materials Science and Engineering Handbook, CRC Press, 2001.
[32] D.J. Lloyd, D. Kenny, Scripta Metal. 22 (1978) 903.
[33] C. Lee, X. Hwei, J.W. Kysar, J. Hone, Science 321 (2008) 385.
[34] K.D. Kepler, J.T. Vaughey, M.M. Thackeray, J. Power Sources 81–82 (1999) 383.
[35] H. Bryngelsson, J. Eskhult, L. Nyholm, K. Edstrom, Electrochim. Acta 53 (2008) 7226.
[36] S. Liang, X. Zhu, P. Lian, W. Yang, H. Wang, J. Solid-State Chem. 184 (2011) 1400.
[37] J. Yao, X.P. Shen, B. Wang, H.K. Liu, G.X. Wang, Electrochem. Commun. 11 (2009) 1849.
[38] P.C. Lian, X.F. Zhu, S.Z. Liang, Z. Li, W.S. Yang, H.H. Wang, Electrochim. Acta 56 (2011) 4532.